Chemical Engineering Journal 498 (2024) 155471

Contents lists available at ScienceDirect

Chemical Engineering Journal

journal homepage: www.elsevier.com/locate/cej

Harnessing donor cyclization strategy: Converting type II to type I photosensitizers and enhancing AIE performance for NIR-II FL/MR imaging-guided photodynamic therapy under hypoxia condition

Chonglu Li [a,d,1], Jie Li [b,c,1], Yida Pang [d,1], Longcan Mei [d,1], Wenhan Xu [d], Zhipeng Zhang [a,*], Cuipin Han [b,c,*], Yao Sun [d,*]

[a] College of Pharmacy, Hubei University of Science & Technology, Xianning 4371000, China
[b] School of Medical Imaging, Xuzhou Medical University, Xuzhou 221004, China
[c] Department of Radiology, Affiliated Hospital of Xuzhou Medical University, Xuzhou 221004, China
[d] State Key Laboratory of Green Pesticide, International Joint Research Center for Intelligent Biosensor Technology and Health, College of Chemistry, Central China Normal University, Wuhan 430079, China

ARTICLE INFO

Keywords:
Donor cyclization strategy
NIR-II FL/MRI imaging
Type I photodynamic therapy
Aggregation-induced emission
Hypoxia

ABSTRACT

Although type I photodynamic therapy (PDT) holds significant advantages in treating hypoxic tumors, limited design strategies for type I photosensitizers, as well as aggregation-caused quenching (ACQ), still hinder its broad application. Herein, a simple donor cyclization strategy is proposed to convert a type II photosensitizer YD-1 into type I photosensitizer YD-2, thereby shifting the predominant ROS production from singlet oxygen ($^1O_2$) to superoxide anion ($O_2^{\bullet-}$). Compared to YD-1, YD-2 demonstrates superior aggregation-induced emission (AIE) performance. Furthermore, by incorporating a magnetic resonance (MR) imaging unit (Gd^{3+}-chelated DOTA) onto the surface of DSPE-mPEG$_{2000}$-NH$_2$-encapsulated YD-2 to construct YD-2-Gd nanoparticles (NPs), which offers much better over single fluorescence (FL) imaging modality. In *vivo,* studies have demonstrated that YD-2-Gd NPs successfully achieved precise and effective PDT for tumors under the guidance of near-infrared-II (NIR-II) FL/MR dual-modal imaging, with no apparent toxic side effects. This work offers a straightforward and effective strategy for improving the precise and efficient treatment of hypoxic solid tumors, providing valuable guidance for designing type I photosensitizers with AIE activity.

1. Introduction

Photodynamic therapy (PDT) is considered to be an effective alternative method for cancer treatment due to its non-invasiveness, high spatiotemporal selectivity, minimal toxic side effects, and the ability to overcome drug resistance [1–5]. Photosensitizers (PSs) are the essential agents for PDT, which generate reactive oxygen species (ROS) upon light irradiation to induce cancer cell death through either type I (electron transfer) or type II (energy transfer) mechanisms [6–12]. The majority of organic PSs primarily generate singlet oxygen ($^1O_2$) through the oxygen (O_2)-dependent type II pathway, resulting in less effective treatment for hypoxic tumors [13–16]. On the other hand, type I PSs exhibit a reduced reliance on O_2 and primarily generate superoxide anions ($O_2^{\bullet-}$) and hydroxyl radicals (•OH), thus offering a potential solution to tumor hypoxia. However, the tedious synthesis of type I organic photosensitizers hinders our understanding of their structure–property relationships [17–20]. Therefore, an easy yet effective strategy is imperative to meet the growing demand for constructing type I PSs, which is greatly beneficial to oncology treatment.

Apart from achieving highly effective PDT, imaging-guided therapeutic strategies are a highly effective method for a trend to fit clinical practice in enhancing the accuracy of tumor localization and metastasis, thereby resulting in enhanced treatment outcomes and reduced adverse reactions [21–26]. MRI is a commonly used imaging tool in clinical diagnosis due to its high spatial resolution and superior soft-tissue visualization [27–29]. Nevertheless, one drawback of MRI is its low sensitivity in distinguishing small lesions from normal tissue. In comparison, optical imaging offers excellent sensitivity and satisfactory

* Corresponding authors at: School of Medical Imaging, Xuzhou Medical University, Xuzhou 221004, China (C. Han).
E-mail addresses: zzplbeckham@foxmail.com (Z. Zhang), hancp@xzhmu.edu.cn (C. Han), sunyaogbasp@mail.ccnu.edu.cn (Y. Sun).
[1] Chonglu Li, Jie Li, Yida Pang, and Longcan Mei contributed equally to this work.

https://doi.org/10.1016/j.cej.2024.155471
Received 1 June 2024; Received in revised form 24 August 2024; Accepted 2 September 2024
Available online 4 September 2024

spatial–temporal resolution [30,31]. In the field of optical imaging, the recent research focus has shifted from the traditional visible-wavelength range (0.4–0.7 μm) to the near-infrared-II (NIR-II, 1.0–1.7 μm) due to the deeper tissue penetration and ultralow auto-fluorescence [32–35]. By utilizing the NIR-II fluorescence imaging, precise images at the cellular or even molecular levels could be obtained [36]. However, the fluorescence of conventional fluorescent PSs would extremely decline under the biological environment due to the aggregation caused quenching (ACQ) effect [37]. The recently emerged aggregation-induced emission (AIE) luminous has fundamentally resolved the sticky issue of fluorescence quenching. Thus, by leveraging the synergistic strengths of two imaging modalities, dual-modal imaging could provide accurate tracing and visualization to guide effective type I PDT for eliminating tumors [38,39]. Given the circumstances, the exploration of an AIEgen to achieve NIR-II FL/MR imaging-guided type-I PDT for tumor treatment is urgently needed.

Herein, we propose a simple donor cyclization strategy to convert type II into type I PSs for NIR-II FL/MR imaging-guided PDT. We design and synthesize a NIR-II AIE PS (YD-1) based on donor–acceptor-donor (D-A-D) skeleton, and cyclize the triphenylamine donor moiety in YD-1 to obtain the corresponding NIR-II AIE type I PS (YD-2) (Scheme 1). Notably, YD-2 exhibits enhanced AIE properties compared to YD-1. Both YD-1 and YD-2 demonstrate robust ROS generation capabilities. Specifically, YD-1 exclusively produces $^1O_2$, while YD-2 selectively generates $O_2^{\bullet-}$ through the type I pathway with low O_2 dependence, which is advantageous for treating hypoxic tumors. Therefore, we employ YD-2 for the subsequent treatment of hypoxic tumors. To enhance biocompatibility and endow MRI capability, photosensitizer YD-2 is encapsulated with DSPE-mPEG$_{2000}$-NH$_2$ and further post-modified with Gd^{3+}-chelated DOTA, enabling the prepared YD-2-Gd NPs suitable for dual-modal imaging. Due to the high density of Gd^{3+} on the surface of the nanoparticles (NPs), the signal intensity in T_1-weighted images is higher than that of conventional commercial contrast agents (Gd-EOB-DTPA). Furthermore, compared to the clinically used indocyanine green (ICG) contrast agent (~3 mm), the fluorescence penetration depth of YD-2-Gd NPs can reach up to ~7 mm. In *vivo,* therapeutic results demonstrate that dual-modal NIR-II FL/MR imaging-guided type I PDT using YD-2-Gd NPs can precisely and effectively eradicate mouse tumors without detectable adverse effects. Therefore, we believe that this work provides a new approach to the designing of type I PS with AIE activity.

2. Materials and methods

Detailed experimental procedures including synthesis, characterization, fluorescence and ROS tests, cytotoxicity tests, and in *vivo* experiments are given in the supporting information.

3. Results and discussion

3.1. Synthesis and photophysical properties

Compounds YD-1 and YD-2 with D-π-A-π-D scaffold were meticulously synthesized via a sequence of classic chemical reactions. Within this scaffold, benzobisthiadiazole (BBTD) served as the electron acceptor unit, and 3,4-ethylenedioxythiophene (EDOT) acted as the π bridge. Triphenylamine and acridine were employed as the electron donor units for YD-1 and YD-2, respectively. All intermediates and final products were identified through nuclear magnetic resonance (NMR) spectroscopy and matrix-assisted laser desorption/ionization time-of-flight mass spectrometry (MALDI-TOF-MS) analysis (Figs. S1–S10). The absorption and emission spectra of YD-1 and YD-2 were measured in dichloromethane (DCM). The maximum absorption for YD-1 and YD-2 were observed at 795 and 730 nm, respectively (Fig. 1A). Additionally, the maximum emission for YD-1 was located at 1105 and for YD-2 at 1000 nm with Stokes shifts of 310 and 270 nm, respectively (Fig. 1B). Compared to YD-1, YD-2 exhibited a noticeable blue shift in both its

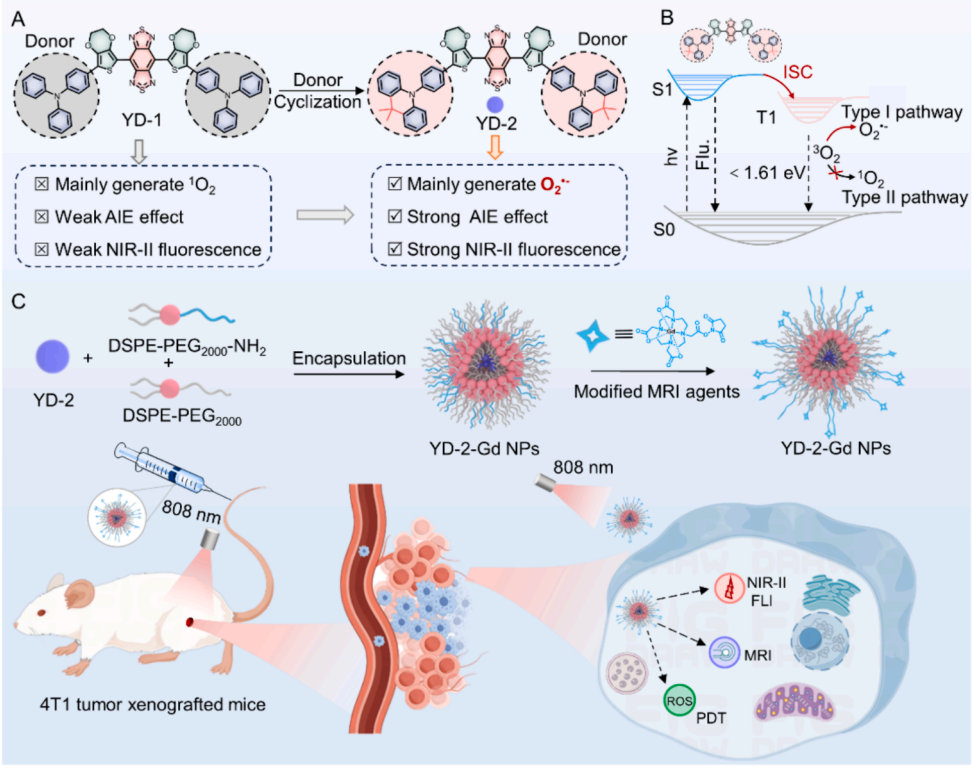

Scheme 1. Schematic diagram of the design and principle of the NIR-II emitted AIE photosensitizer and FL/MRI imaging-guided PDT. (A) Chemical structure and design strategy of type I NIR-II emitting AIE photosensitizer. (B) Schematic illustration of the coordinated photophysical processes and generation of $O_2^{\bullet-}$ by YD-2 upon photoexcitation. (C) Preparation Process of YD-2-Gd NPs and application in dual-modal FL/MRI imaging-guided PDT.

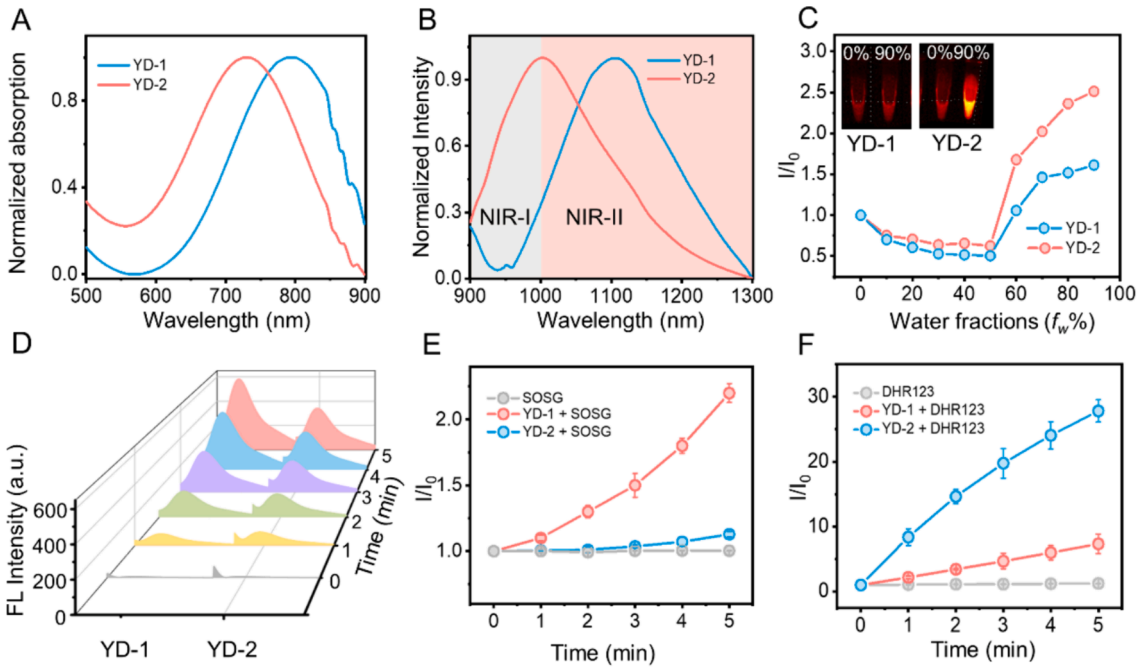

Fig. 1. Characterization and properties of the compounds. (A) Normalized absorption spectra and (B) normalized emission spectra of YD-1 and YD-2 in DCM solution. (C) Plots of relative fluorescence intensity (I/I_0) of YD-1 at 1105 nm and YD-2 at 1000 nm with varying water fractions. Inset: NIR-II fluorescence images (1000 LP, 808 nm excitation, 28 mW/cm^2, 5 ms) of YD-1 and YD-2 in DMSO and DMSO/water (f_w = 90 %). (D) ROS generation of YD-1 (15 μM) and YD-1 (15 μM) under 808 nm laser irradiation (1 W/ cm^2) for different times. (E) SOSG, and (F) DHR123 fluorescence enhancement in the presence of YD-1(15 μM) and YD-2(15 μM) under 808 nm laser irradiation. Values were expressed as the mean ± SD (n = 3).

maximum absorption and emission peaks. This shift can likely be attributed to the cyclization of triphenylamine, which effectively reduces the coplanarity of the entire D-π-A-π-D molecule [33,40,41]. Then, the AIE characteristics of YD-1 and YD-2 using dimethyl sulfoxide (DMSO) as a good solvent and water as a bad solvent were further investigated. As shown in Fig. 1C, the FL intensity of both YD-1 and YD-2 gradually decreases as water fraction (f_w) increased from 0 to 50 %, while experiencing a significant increase from 50 % to 90 %. Additionally, as f_w increased to 90 %, the fluorescence intensity of YD-1 enhanced by ~1.2-fold compared to that of pure DMSO, while the fluorescence intensity of YD-2 improved by ~2.5-fold (Fig. 1C). These findings suggest that compared to YD-1, YD-2 exhibits superior AIE performance. This improvement was likely due to YD-2′s more twisted conformation, which suppresses intermolecular interactions during aggregation. Additionally, the restriction of rotatable and vibrational units following TPA cyclization further enhances its AIE performance [42–44].

3.2. ROS generation and theoretical calculation

Subsequently, the ROS generation capacity of YD-1 and YD-2 was assessed. The total ROS generation capacity of YD-1 and YD-2 in the DMSO solution was investigated by using 2′,7′-dichlorodihydrofluorescein (DCFH) as an indicator. DCFH can be oxidized by various ROS to form dichlorofluorescin (DCF, λ_m = 525 nm), to emit green fluorescence. Due to the strong absorption of the synthesized AIE photosensitizers in the NIR region, an 808 nm laser was employed as the PDT light source. As illustrated in Fig. 1D and Fig. S11, in the presence of either YD-1 or YD-2, the fluorescence intensity of DCF significantly increased under laser irradiation (1 mW/cm^2), while DCFH alone showed no significant change under laser irradiation. After 5 min of laser exposure, the DCF fluorescence intensity increased by ~76-fold and ~47-fold in the presence of YD-1 and YD-2, respectively, indicating excellent ROS generation capability (Fig. 1D and Fig. S11). Furthermore, the ROS generation capability of YD-2 was lower than that of YD-1, possibly due to the cyclization of triphenylamine suppressing the ICT effect of the entire molecule. To further clarify the types of generated ROS, we employed three free radical indicators, namely singlet oxygen sensor green (SOSG), dihydrorhodamine 123 (DHR123), and hydroxyphenyl fluorescein (HPF), for detecting $^1O_2$, $O_2^{\bullet-}$, and •OH, respectively. As shown in Fig. 1E and Fig. S12, when the mixture of SOSG and YD-1 was irradiated with an 808 nm laser (1 W/cm^2, 5 min), a significant increase in fluorescence intensity at 533 nm was observed for SOSG, while YD-2 showed almost no change. These results indicated that YD-1 mainly generated $^1O_2$, while YD-2 hardly produced $^1O_2$. This result was further confirmed by 9,10-anthracenediyl-bis(methylene) dimalonic acid (ABDA) indicators (Fig. S13) Surprisingly, when DHR123 was treated with YD-2 and laser irradiation, a sharp increase in fluorescence intensity at 530 nm was observed, while YD-1 had almost no apparent effect (Fig. 1F and Fig. S14). This suggested that YD-2 primarily generated $O_2^{\bullet-}$, whereas YD-1 showed minimal capability to produce $O_2^{\bullet-}$. This result was further confirmed by dihydroethidium (DHE) fluorescent indicators (Fig. S15). Furthermore, the fluorescence intensity of HPF at 520 nm was negligible after treatment with either YD-1 or YD-2, under laser irradiation, indicating that neither of them had the ability to •OH (Fig. S16). To further confirm the types of ROS generated by YD-1 and YD-2 under laser irradiation, electron paramagnetic resonance (EPR) experiments were conducted using 2,2,6,6-tetramethylpiperidine (TEMP) and 5,5-dimethyl-1-pyrroline N-oxide (DMPO) as spin traps. As illustrated in Fig. S17, YD-1 exclusively exhibits a distinct $^1O_2$ signal characteristic, whereas YD-2 exclusively shows a distinct $O_2^{\bullet-}$signal characteristic. Time-resolved fluorescence spectroscopy reveals that both YD-1 and YD-2 had relatively short fluorescence lifetimes (Fig. S18). Notably, YD-2 exhibited a shorter fluorescence lifetime (328 ps) compared to YD-1 (684 ps). This suggests that under 808 nm laser irradiation, YD-2 underwent a faster electron transfer process, thereby enhancing the Type I PDT pathway. Furthermore, we conducted photocurrent experiments to evaluate the charge separation abilities of YD-1 and YD-2. The results showed a significant increase in photocurrent for YD-2 compared to YD-1 (Fig. S19),

indicating that YD-2 had a higher charge transfer rate, which favored electron transfer to produce type-I ROS. These results implied that through a simple triphenylamine cyclization, a type II PS could be converted into a type I PS. Additionally, the photothermal effects of YD-1 and YD-2 were investigated. As shown in Fig. S20, after 808 nm laser irradiation for 5 min, the temperature of both YD-1 and YD-2 gradually increased with increasing concentration, reaching peaks exceeding 50 °C. This demonstrated their good photothermal effects, which were beneficial for subsequent tumor treatments.

To further investigate the mechanism of converting type II to type I PSs, theoretical calculations were conducted for YD-1 and YD-2 using density functional theory (DFT) at the B3LYP/6-311++G(d, p) level (Table S1 and S2). As shown in Fig. 2A and B, compared to YD-1, the dihedral angle between the EDOT and the BBTD core in YD-2 after TPA cyclization increased to 39.5° (38.8° for YD-1). Notably, after TPA cyclization, the acridine group was almost perpendicular to the BBTD core, with a dihedral angle of 89.4°. These changes reduced the coplanar conformation of YD-2, which may explain the blue shift in the emission wavelength and the more pronounced AIE effect observed in YD-2. Further studies on the molecular orbitals of these two molecules demonstrated that the lowest unoccupied molecular orbitals (LUMO) electron clouds of YD-1 and YD-2 were predominantly distributed over the benzothiadiazole moiety, while the highest occupied molecular orbital (HOMO) was mainly contributed by the orbitals of triphenylamine and acridine, indicating a well-separated HOMO-LUMO characteristic. The HOMO-LUMO energy gap increased from 1.70 eV (YD-1) to 1.78 eV (YD-2), resulting in a blue shift in the absorption spectra of YD-2, consistent with the experimental data (Fig. 2C). Furthermore, YD-1 (0.07 eV) and YD-2 (0.22 eV) possessed relatively narrow energy gap (ΔE_{ST}) between the S_1 and T_1 states, which was conducive to the generate ROS (Fig. 2C). Additionally, it was found that the energy difference from T_1 to S_0 ($\Delta E_{T1\text{-}S0}$) between $^3O_2$ and $^1O_2$ (1.61 eV from TD-DFT calculation) [17,45–47] was higher than that of YD-2 but lower than YD-1 (Fig. 2C). This result indicated that YD-2 exhibited a lower efficiency in type II energy transfer, thus elucidating its reduced production capacity of $^1O_2$. Taken together, these theoretical data were consistent with the experimental results described above, further supporting the successful conversion of type II to type I PSs through the donor cyclization strategy.

3.3. Preparation and characterization of YD-2-Gd NPs

Based on the above description, we chose YD-2 for further research because it exhibits superior type I PDT and NIR-II AIE performance compared to YD-1. To endow YD-2 with MRI capability and enhanced biocompatibility, YD-2 was encapsulated to form uniform NPs using DSPE-mPEG$_{2000}$ and DSPE-mPEG$_{2000}$-NH$_2$. Subsequently, DOTA-Gd (an MRI contrast agent) was covalently modified onto the surface of the NPs through amine and active ester reactions to prepare YD-2-Gd NPs (Fig. 3A). The results of dynamic light scattering (DLS) measurements and transmission electron microscopy (TEM) imaging revealed that YD-2-Gd NPs formed uniformly spherical nanoparticles with an approximate diameter of ~61 nm (Fig. 3B). Such nanoscale particles are conducive to the enhanced permeability and retention (EPR) effect at tumor sites. As depicted in Fig. 3C and Figs. S21 and S22, YD-2-Gd NPs exhibited excellent stability in ultrapure water, phosphate-buffered saline (PBS), and 10 % fetal bovine serum (FBS) in 90 % PBS. Compared to the DCM solution, the absorption and fluorescence spectra of YD-2-Gd NPs exhibited a blue shift trend in water, with maximum peaks located at 705 nm and 995 nm, respectively (Fig. 3D). To assess the optical penetration ability of YD-2-Gd NPs, a liquid containing 1 % intralipid was utilized to simulate tissue thickness under physiological conditions. Due to their longer emission wavelength and excellent NIR-II fluorescence performance, the penetration depth of YD-2-Gd NPs can

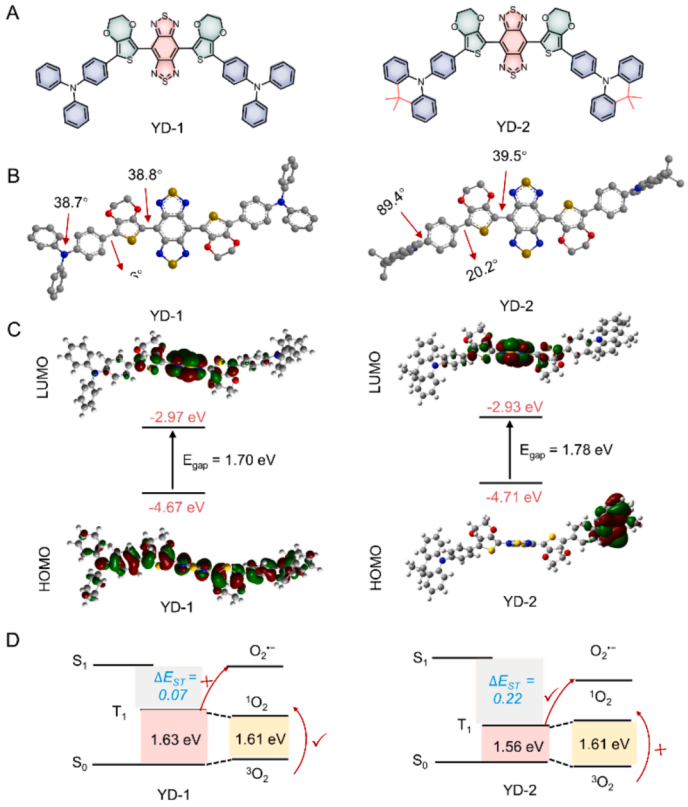

Fig. 2. Theoretical calculation. (A) Chemical structure of YD-1 and YD-2. (B) Optimized S_0 geometries of YD-1 and YD-2. (C) Frontier molecular orbital diagram of LUMO and HOMO determined at the theoretical B3LYP/6–311++G(d, p) level. (D) Energy profile for a putative type II energy transfer from the T_1 level of YD-1 and YD-2 to $^3O_2$.

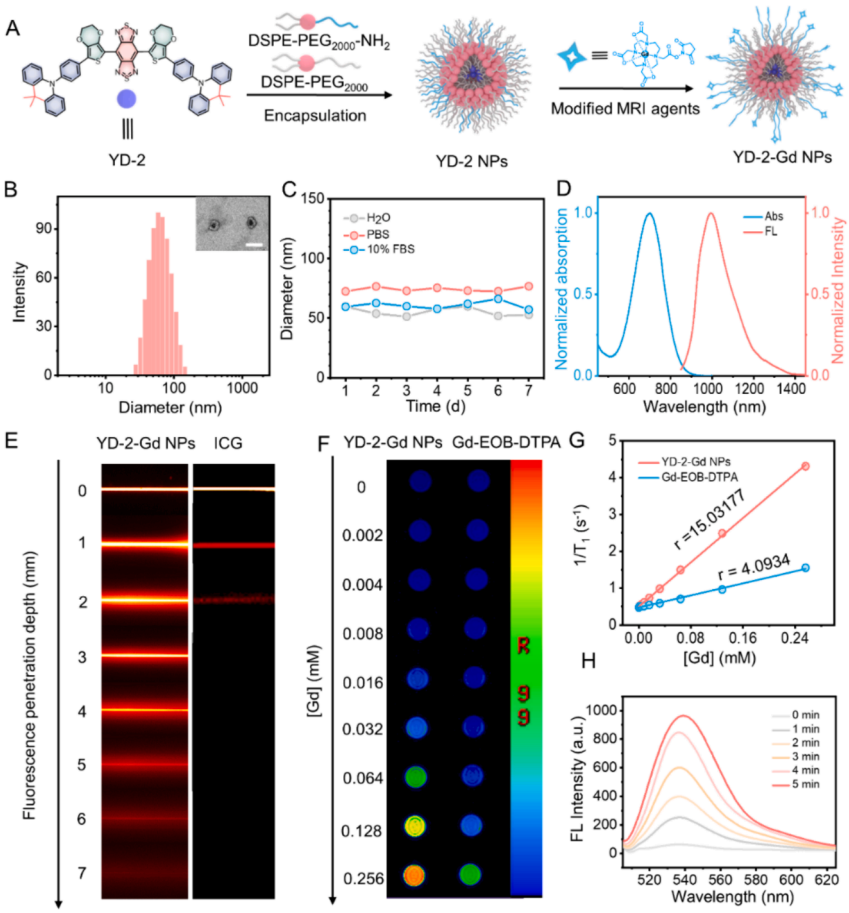

Fig. 3. Characterization and properties of YD-2-Gd NPs. (A) Preparation schematic of DSPE-mPEG$_{2000}$ and DSPE-mPEG$_{2000}$-NH$_2$ encapsulating YD-2 and covalently modifying DOTA-Gd to form YD-2-Gd NPs. (B) DLS distribution of YD-2-Gd NPs in aqueous solution. Inset: TEM image of YD-2-Gd NPs. Scale bar: 50 nm. (C) DLS analysis of the stability of YD-2-Gd NPs in pure water, PBS, or 10 % FBS solution. (D) Normalized absorption and emission spectra of YD-2-Gd NPs in aqueous solution. (E) NIR-II fluorescence images of YD-2-Gd NPs and ICG in a capillary tube under different depths of 1 % intralipid (28 mW/cm^2, 150 ms, LP 1000). (F) T_1-weighted MR images of YD-2-Gd NPs and Gd-EOB-DTPA at different Gd^{3+} concentrations. (G) Effective r_1 relativities of YD-2-Gd NPs and Gd-EOB-DTPA. (H) Fluorescence spectrum of the solution of YD-2-Gd NPs (15 μM) and DHR123 (20 μM) under 808 nm laser irradiation (1 W/ cm^2) for different times.

reach ~7 mm, compared to only ~3 mm for ICG (the US Food and Drug Administration (FDA)-approved agent) (Fig. 3E). To investigate the MRI performance of YD-2-Gd NPs, we conducted a comparison with the commercial contrast agent Pomex (Gd-EOB-DTPA). Both YD-2-Gd NPs and Gd-EOB-DTPA exhibited an increase in signal intensity on T_1-weighted MR images with increasing concentration (Fig. 3F). At equivalent concentrations of Gd^{3+}, the magnetic resonance signal of YD-2-Gd NPs surpassed that of Gd-EOB-DTPA. The r_1 relativity of YD-2-Gd NPs is 15.03 ± 0.12 $mM^{-1}s^{-1}$, which was 3.6-folds higher than that of Gd-EOB-DTPA (4.09 ± 0.09 $mM^{-1}s^{-1}$) (Fig. 3G). Subsequently, aiming to confirm that the encapsulation of DSPE-mPEG$_{2000}$ would not affect the ROS generation performance of YD-2, we further investigated the ROS generation capability and types of YD-2-Gd NPs. As depicted in Fig. S23, YD-2-Gd NPs also exhibited efficient ROS generation. Additionally, under 808 nm laser irradiation, YD-2-Gd NPs exclusively produce $O_2^{\bullet-}$ (Fig. 3H), with minimal production of $^1O_2$ and •OH (Figs. S24 and S25), suggesting that the encapsulation of DSPE-mPEG$_{2000}$ does not alter the PDT type of photosensitizer YD-2.

3.4. *In vitro anticancer efficacy study*

First, the uptake of YD-2-Gd NPs by cancer cells was investigated. As shown in Fig. 4A and Fig. S26, after incubating 4 T1 cells with YD-2-Gd NPs for 2 h, the NIR-II fluorescence within the cells reached its maximum. With prolonged incubation time, the corresponding average fluorescence intensity within the cells gradually decreased. Subsequently, the dark cytotoxicity of YD-2-Gd NPs on normal cells was evaluated through CCK-8 assay. After incubating L-02 and 16HBE cells with varying concentrations of YD-2-Gd NPs for 12 h, the cell viability remained above 85 % for both cell lines, indicating excellent biocompatibility of YD-2-Gd NPs (Fig. S27).

Given the excellent type I photodynamic performance of YD-2-Gd NPs, we further evaluated their cytotoxicity against 4 T1 cells under normoxic and hypoxic conditions using the CCK-8 assay. As depicted in Fig. 4B,C and Fig. S28, under dark conditions, YD-1-Gd NPs and YD-2-Gd NPs exhibited almost no toxicity to 4 T1 cells. After irradiation with an 808 nm laser for 5 min, the antitumor capability of YD-1-Gd NPs was higher than that of YD-2-Gd NPs under normoxic conditions (Fig. 4B,C and Fig. S28). However, under hypoxic conditions, the antitumor capability of YD-1-Gd NPs was significantly reduced (Fig. S28). In contrast, YD-2-Gd NPs exhibited good antitumor effects under both normoxic and hypoxic conditions (Fig. 4B and C). These results indicated that YD-2-Gd NPs had the capability to overcome the hypoxic tumor microenvironment. To assess the degree of cytotoxicity mediated by PDT or photothermal therapy (PTT), N-acetylcysteine (NAC, an effective ROS scavenger) and an ice bath (to inhibit heat generation) were used in the CCK-8 assay. Under normoxic conditions, after treating 4 T1 cells with YD-2-Gd NPs and 808 nm laser irradiation, the survival rate of NAC-pretreated cells increased from ~21 % to ~67 %, while the survival rate of ice bath-pretreated cells increased only to ~34 %. This

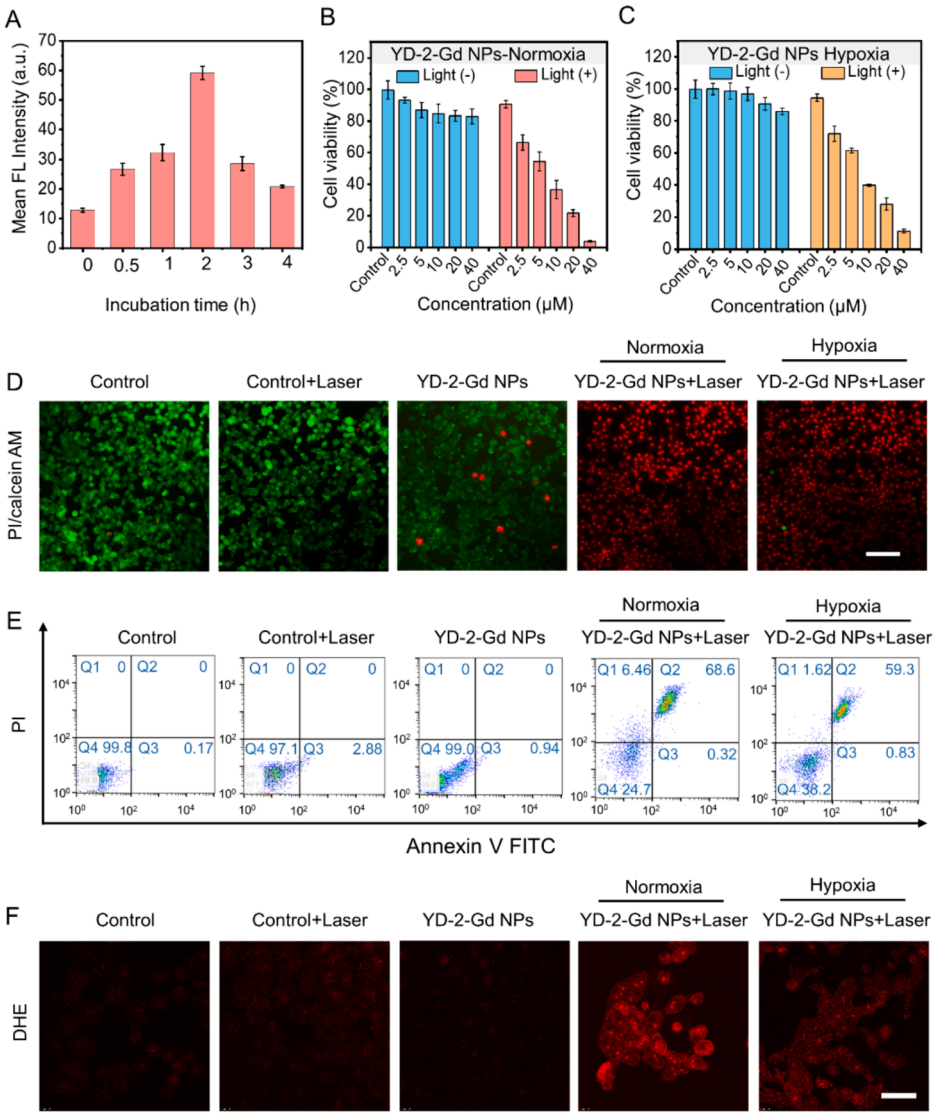

Fig. 4. In *vitro* anticancer efficacy study. (A) Semi-quantitative analysis of 4 T1 cells with NIR-II fluorescence imaging. The cell viability of 4 T1 cells was incubated with different concentrations of YD-2-Gd NPs for 8 h in either (B) normoxic or (C) hypoxic conditions under 808 nm laser irradiation (1 W/cm^2, 5 min). (D) Live/dead images of 4 T1 cells after different treatments. Scale bar: 500 μm. (E) The cell apoptosis rate of 4 T1 cells after different treatments was analyzed by flow cytometry. (F) Confocal imaging of intracellular $O_2^{\bullet-}$ production under different conditions by using DHE staining. Scale bar: 50 μm.

indicated that the anticancer effect of YD-2-Gd NPs was primarily due to the PDT effect. Under hypoxic conditions, the experimental results showed a similar trend (Fig. S29). To visually demonstrate the cytotoxicity of YD-2-Gd NPs, calcein AM (green) and propidium iodide (PI) were used to stain live cells (green fluorescence) and dead cells (red fluorescence), respectively. As shown in Fig. 4D and Fig. S30, under 808 nm laser irradiation, YD-2-Gd NPs exhibited bright red fluorescence in 4 T1 cells under normoxic/hypoxic conditions, indicating their excellent ability to eliminate tumor cells.

To observe the apoptotic effect induced by YD-2-Gd NPs on tumor cells, we conducted a quantitative analysis using flow cytometry. As illustrated in Fig. 4E, under normoxic/hypoxic conditions, YD-2-Gd NP-treated 4 T1 cells exhibited an apoptotic rate exceeding 59 % with laser irradiation. Subsequently, the ROS generation ability of YD-2-Gd NPs was assessed at the cellular level. Although under normoxic conditions, 4 T1 cells treated with YD-1-Gd NPs exhibited a more pronounced DCF green fluorescence signal compared to 4 T1 cells treated with YD-2-Gd NPs, under hypoxic conditions, the green fluorescence signal in cells treated with YD-1-Gd NPs was significantly weaker than that in cells treated with YD-2-Gd NPs (Fig. S31). Moreover, the production of $O_2^{\bullet-}$ was confirmed at the cellular level using the DHE probe. As shown in the Fig. 4F and Fig. S32, under 808 nm laser irradiation, 4 T1 cells treated with YD-2-Gd NPs displayed significant DHE red fluorescence under both normoxic and hypoxic conditions, whereas no similar results were observed for YD-1-Gd NPs. This finding indicates the outstanding ability of YD-2-Gd NPs to induce tumor cells apoptosis even under hypoxic conditions.

3.5. NIR-II FL/MR imaging-guided PDT in vivo

Given the excellent NIR-II FLI/MRI capabilities and PDT performance of YD-2-Gd NPs, we further assessed their tumor therapeutic potential guided by in *vivo* FL/MR imaging. Before this, we first investigated the biocompatibility of YD-2-Gd NPs through a hemolysis assay and found no significant hemolytic effect (Fig. S33). Additionally, we determined that the half-life of YD-2-Gd NPs in blood was 12 h, confirming their relatively long circulation time *in vivo* (Fig. S34). Subsequently, we evaluated their NIR-II FL/MR imaging capabilities at the in

vivo level (Fig. 5A). After YD-2-Gd NPs were intravenously injected into 4 T1 tumor-bearing BALB/c mice, the fluorescence signal at the tumor site gradually increased over time, peaking at 8 h post-injection (Fig. 5B). Concurrently, T_1-weighted MR imaging showed the highest signal intensity at 8 h post-injection (Fig. 5C), showing a relatively good consistency between the fluorescence signal and the MR intensity at the tumor site (Fig. 5D).

Additionally, the *ex vivo* biodistribution of YD-2-Gd NPs was investigated 24 h postinjection (Fig. S35). The results showed high fluorescence intensity in the tumor, liver, and spleen, indicating that YD-2-Gd NPs were mainly metabolized by the hepatobiliary system. Subsequently, we evaluated the in *vivo* anti-tumor activity of YD-2-Gd NPs by monitoring tumor growth in 4 T1 tumor-bearing mice. After intravenous injection of PBS or YD-2-Gd NPs for 8 h, the mice were subjected to 5 min of irradiation with an 808 nm laser (1 W/cm^2). As depicted in Fig. 5E and Fig. S36, the tumor volume in the control groups, control + laser groups and YD-2-Gd NPs alone exhibited rapid increases during the treatment period. Conversely, under 808 nm laser irradiation, YD-2-Gd NPs effectively suppressed tumor growth even 23 days post-treatment, demonstrating their remarkable anti-tumor efficacy (Fig. 5E and Fig. S36). Furthermore, we investigated their in vivo anti-cancer mechanism through tumor histology. As shown in Fig. 5F, hematoxylin-eosin (H&E) and terminal deoxynucleotidyl transferase-mediated dUTP nick-end labeled (TUNEL) staining of tumor sections revealed a significant presence of tumor cell apoptosis in tumors treated with YD-2-Gd NPs plus laser irradiation compared to other control groups. These results demonstrated that YD-2-Cd NPs effectively enabled NIR-II FL/MR- imaging guided type I PDT.

To evaluate the *in vivo* biosafety of YD-2-Gd NPs, we monitored the mouse body weight during treatment. As depicted in Fig. S37, there was no significant weight loss observed in mice during the observation time. Blood routine tests were conducted on experimental mice, revealing normal levels of liver function indicators (ALT, ALP, AST, ALB) and kidney function indicators (CREA, BUN) after YD-2-Gd NPs treatment (Fig. S38). Furthermore, H&E staining revealed no discernible signs of abnormal tissue morphology or pathology in the major organs (hearts, livers, spleens, lungs, and kidneys) of all experimental mice in different groups (Fig. S39). These findings indicate that YD-2-Gd NPs exhibited excellent biosafety.

4. Conclusion

In summary, we propose a simple donor cyclization strategy to convert type II PSs into type I PSs. Under light irradiation, YD-1 primarily generated $^1O_2$, while donor-cyclized YD-2 predominantly produced $O_2^{\bullet-}$, which was rarely dependent on the O_2 concentration in the hypoxic tumor microenvironment. Furthermore, by modifying an MRI imaging unit (DOTA chelated with Gd^{3+}) onto the surface of DSPE-mPEG$_{2000}$-NH$_2$ encapsulated YD-2, we resolve the issue of insufficient spatial resolution in single fluorescence imaging. The highly aggregated Gd^{3+} on the surface of NPs enhanced the signal in T_1-weighted images compared to commercial contrast agents (Gd-EOB-DTPA). In vivo therapeutic experiments demonstrate that YD-2-Gd NPs achieve precise and effective type I PDT guided by NIR-II FL/MR dual-modal imaging in mice tumor model, with no apparent toxic side effects. This study presents a simple and effective strategy to enhance the precise and efficient treatment of hypoxic solid tumors, offering valuable guidance for the design of multifunctional type I PSs in the NIR-II region [48].

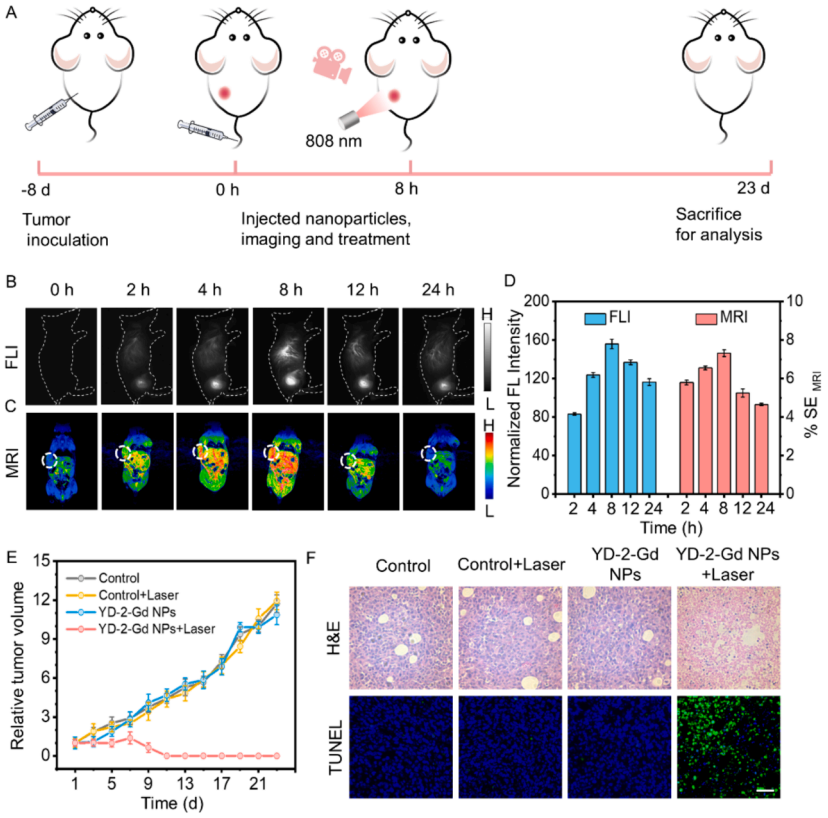

Fig. 5. NIR-II FL/MRI imaging-guided PDT in *vivo*. (A) Schematic diagram of tumor treatment in mice. (B) NIR-II fluorescence of 4 T1 tumor-bearing mice after the injection of YD-2-Gd NPs. (C) T_1-weighted MR image of 4 T1 tumor-bearing mice after the injection of YD-2-Gd NPs. (D) Semi-quantitative analysis of FLI and MRI. (E) Tumor growth curves of 4 T1 tumor-bearing mice with different treatments. (F) H&E and TUNEL staining analysis of tumor tissues after various treatments. Scale bar: 100 μm.

CRediT authorship contribution statement

Chonglu Li: Writing – original draft, Project administration. **Jie Li:** Software, Methodology. **Yida Pang:** Visualization, Validation. **Longcan Mei:** Software, Methodology. **Wenhan Xu:** Formal analysis. **Zhipeng Zhang:** Visualization, Validation, Resources. **Cuipin Han:** Validation, Resources, Formal analysis, Data curation. **Yao Sun:** Writing – review & editing, Project administration, Investigation, Conceptualization.

Declaration of competing interest

The authors declare that they have no known competing financial interests or personal relationships that could have appeared to influence the work reported in this paper.

Data availability

Data will be made available on request.

Acknowledgments

This work was financially supported by the National Natural Science Foundation of China (No. 22022404, 22074050, 22374055), the National Natural Science Foundation of Hubei Province (2022CFA033), the National Science Foundation of Jiangsu Province (BK20231165), the Fundamental Research Funds for the Central Universities (CCNU22QN007). All animals in this study were handled according to a protocol approved by the Institutional Animal Care and Use Committee of Central China Normal University.

Appendix A. Supplementary data

Supplementary data to this article can be found online at https://doi.org/10.1016/j.cej.2024.155471.

References

[1] S. Monro, K.L. Colón, H.M. Yin, J. Roque, P. Konda, S. Gujar, R.P. Thummel, L. Lilge, C.G. Cameron, S.A. McFarland, Transition metal complexes and photodynamic therapy from a tumor-centered approach: challenges, opportunities, and highlights from the development of TLD1433, Chem. Rev. 119 (2019) 797–828, https://doi.org/10.1021/acs.chemrev.8b00211.
[2] M. Piksa, C. Lian, I.C. Samuel, K.J. Pawlik, I.D.W. Samuel, K. Matczyszyn, The role of the light source in antimicrobial photodynamic therapy, Chem. Soc. Rev. 52 (2023) 1697–1722, https://doi.org/10.1039/D0CS01051K.
[3] T.C. Pham, V.N. Nguyen, Y. Choi, S. Lee, J. Yoon, Recent strategies to develop innovative photosensitizers for enhanced photodynamic therapy, Chem. Rev. 121 (2021) 13454–13619, https://doi.org/10.1021/acs.chemrev.1c00381.
[4] X.Z. Zhao, J.P. Liu, J.L. Fan, H. Chao, X.J. Peng, Recent progress in photosensitizers for overcoming the challenges of photodynamic therapy: from molecular design to application, Chem. Soc. Rev. 50 (2021) 4185–4219, https://doi.org/10.1039/D0CS00173B.
[5] C.L. Li, Y.D. Pang, Y.L. Xu, M.J. Lu, L. Tu, Q. Li, A. Sharma, Z.Z. Guo, X.Y. Li, Y. Sun, Near-infrared metal agents assisting precision medicine: from strategic design to bioimaging and therapeutic applications, Chem. Soc. Rev. 52 (2023) 4392–4442, https://doi.org/10.1039/D3CS00227F.
[6] X.Y. Liu, W.J. Zhan, G. Gao, Q.C. Jiang, X.P. Zhang, H.B. Zhang, X.B. Sun, W. Han, F.G. Wu, G.L. Liang, Apoptosis-amplified assembly of porphyrin nanofiber enhances photodynamic therapy of oral tumor, J. Am. Chem. Soc. 145 (2023) 7918–7930, https://doi.org/10.1021/jacs.2c13189.
[7] C.Y. Huang, T.F. Zhang, Y. Li, M. Lyu, M. Suo, L.G. Xia, L.R. Liu, B.Z. Tang, Q. Q. Zhang, Type-I AIE photosensitizer triggered cascade catalysis system for tumor targeted therapy and postoperative recurrence suppression, Chem. Eng. J. 446 (2022) 136381, https://doi.org/10.1016/j.cej.2022.136381.
[8] T. Xiong, Y.C. Chen, Q. Peng, S. Lu, S.R. Long, M.L. Li, H. Wang, S. Lu, X.Q. Chen, J. L. Fan, L. Wang, X.J. Peng, Lipid droplet targeting type i photosensitizer for ferroptosis via lipid peroxidation accumulation, Adv. Mater. 36 (2024) 2309711, https://doi.org/10.1002/adma.202309711.
[9] L. Yu, Y. Xu, Z.J. Pu, H. Kang, M. Li, J.L. Sessler, J.S. Kim, Photocatalytic superoxide radical generator that induces pyroptosis in cancer cells, J. Am. Chem. Soc. 144 (2022) 11326–11337, https://doi.org/10.1021/jacs.2c03256.
[10] Y.L. Li, D. Zhang, Y.W. Yu, L. Zhang, L. Li, L.L. Shi, G.X. Feng, B.Z. Tang, A cascade strategy boosting hydroxyl radical generation with aggregation-induced emission photosensitizers-albumin complex for photodynamic therapy, ACS Nano 17 (2023) 16993–17003, https://doi.org/10.1021/acsnano.3c04256.
[11] Y.L. Xu, Y.D. Pang, L.S. Luo, A. Sharma, J.F. Yang, C.L. Li, S. Liu, J.B. Zhan, Y. Sun, De novo designed Ru(II) metallacycle as a microenvironment-adaptive sonosensitizer and sonocatalyst for multidrug-resistant biofilms eradication, Angew. Chem. Int. Ed. 63 (2024) e202319966, https://doi.org/10.1002/anie.202319966.
[12] L. Huang, D.Y. Qing, S.J. Zhao, X.L. Wu, K. Yang, X.J. Ren, X.L. Zheng, M.H. Lan, J. Ye, L.T. Zeng, G.L. Niu, Acceptor-donor-acceptor structured deep-red AIE photosensitizer: lysosome-specific targeting, long-term imaging, and effective photodynamic therapy, Chem. Eng. J. 430 (2022) 132638, https://doi.org/10.1016/j.cej.2021.132638.
[13] Q. Wan, R.Y. Zhang, Z.Y. Zhuang, Y.X. Li, Z.M. Wang, W.J. Zhang, J.Q. Hou, B. Z. Tang, Molecular engineering to boost aie-active free radical photogenerators and enable high-performance photodynamic therapy under hypoxia, Adv. Funct. Mater. 34 (2024) 2312870, https://doi.org/10.1002/adfm.202312870.
[14] S.S. Wang, L.Z. Gai, Y.C. Chen, X.B. Ji, H. Lu, Z.J. Guo, Mitochondria-targeted BODIPY dyes for small molecule recognition, bio-imaging and photodynamic therapy, Chem. Soc. Rev. 53 (2024) 3976–4019, https://doi.org/10.1039/D3CS00456B.
[15] L. Tu, C.L. Li, Q.H. Ding, A. Sharma, M.Q. Li, J.R. Li, J.S. Kim, Y. Sun, Augmenting cancer therapy with a supramolecular immunogenic cell death inducer: a lysosome-targeted nir-light-activated ruthenium(ii) metallacycle, J. Am. Chem. Soc. 146 (2024) 8991–9003, https://doi.org/10.1021/jacs.3c13224.
[16] Y.J. Wang, H.X. Shen, Z. Li, S.Y. Liao, B.L. Yin, R.Y. Yue, G.Q. Guan, B.D. Chen, G. S. Song, Enhancing fractionated cancer therapy: a triple-anthracene photosensitizer unleashes long-persistent photodynamic and luminous efficacy, J. Am. Chem. Soc. 146 (2024) 6252–6265, https://doi.org/10.1021/jacs.3c14387.
[17] M. Zhao, Y.Y. Zhang, J. Miao, H. Zhou, Y. Jiang, Y. Zhang, M.Q. Miao, W. Chen, W. Xing, Q. Li, Q.Q. Miao, An activatable phototheranostic probe for anti-hypoxic type i photodynamic-and immuno-therapy of cancer, Adv. Mater. 36 (2024) 2305243, https://doi.org/10.1002/adma.202305243.
[18] T.F. Zhang, Y.L. Deng, Y.S. Liu, S.L. Chua, B.Z. Tang, B.L. Khoo, Bacterial targeted AIE photosensitizers synergistically promote chemotherapy for the treatment of inflammatory cancer, Chem. Eng. J. 447 (2022) 137579, https://doi.org/10.1016/j.cej.2022.137579.
[19] X. Zhao, Q.C. Yao, S. Long, W.J. Chi, Y.X. Yang, D. Tan, X.G. Liu, H.Q. Huang, W. Sun, J.J. Du, J.L. Fan, X.J. Peng, An approach to developing cyanines with simultaneous intersystem crossing enhancement and excited-state lifetime elongation for photodynamic antitumor metastasis, J. Am. Chem. Soc. 143 (2021) 12345–12354, https://doi.org/10.1021/jacs.1c06275.
[20] X.Z. Zhao, S.R. Long, M.L. Li, J.F. Cao, Y.C. Li, L.Y. Guo, W. Sun, J.J. Du, J.L. Fan, X.J. Peng, Oxygen-dependent regulation of excited-state deactivation process of rational photosensitizer for smart phototherapy, J. Am. Chem. Soc. 142 (2020) 1510–1517, https://doi.org/10.1021/jacs.9b11800.
[21] P.H. Xiao, Z.P. Shen, D.L. Wang, Y.Z. Pan, Y. Li, J.Y. Gong, L. Wang, D. Wang, B. Z. Tang, Precise molecular engineering of type i photosensitizers with near-infrared aggregation-induced emission for image-guided photodynamic killing of multidrug-resistant bacteria, Adv. Sci. 9 (2022) 2104079, https://doi.org/10.1002/advs.202104079.
[22] L. Zhang, A. Song, Q.C. Yang, S.J. Li, S. Wang, S.C. Wan, J.W. Sun, R.T.K. Kwok, J. W.Y. Lam, H.X. Deng, B.Z. Tang, Z.J. Sun, Integration of AIEgens into covalent organic frameworks for pyroptosis and ferroptosis primed cancer immunotherapy, Nat. Commun. 14 (2023) 5355, https://doi.org/10.1038/s41467-023-41121-z.
[23] Y.L. Xu, C.L. Li, S. Lu, Z.Z. Wang, S. Liu, X.J. Yu, X.P. Li, Y. Sun, Construction of emissive ruthenium(II) metallacycle over 1000 nm wavelength for in vivo biomedical applications, Nat. Commun. 13 (2022) 2009, https://doi.org/10.1038/s41467-022-29572-2.
[24] M.L. Liu, Y.C. Chen, Y. Guo, H. Yuan, T.X. Cui, S.K. Yao, S.X. Jin, H.H. Fan, C. J. Wang, R. Xie, W.J. He, Z.J. Guo, Golgi apparatus-targeted aggregation-induced emission luminogens for effective cancer photodynamic therapy, Nat. Commun. 13 (2022) 2179, https://doi.org/10.1038/s41467-022-29872-7.
[25] C.L. Li, L. Tu, Y.L. Xu, M.Q. Li, J.X. Du, P.J. Stang, Y. Sun, Y. Sun, A NIR-light-activated and lysosomal-targeted Pt(II) metallacycle for highly potent evoking of immunogenic cell death that potentiates cancer immunotherapy of deep-seated tumors, Angew. Chem. Int. Ed. (2024) e202406392, https://doi.org/10.1002/anie.202406392.
[26] H. Li, Y. Kim, H. Jung, J.Y. Hyun, I. Shin, Near-infrared (NIR) fluorescence-emitting small organic molecules for cancer imaging and therapy, Chem. Soc. Rev. 51 (2022) 8957–9008, https://doi.org/10.1039/D2CS00722C.
[27] Y.Q. Wang, H. Bai, Y.X. Miao, J.H. Weng, Z. Huang, J.Y. Fu, Y. Zhang, J.G. Lin, D. J. Ye, Tailoring a near-infrared macrocyclization scaffold allows the control of in situ self-assembly for photoacoustic/pet bimodal imaging, Angew. Chem. Int. Ed. 61 (2022) e202200369, https://doi.org/10.1002/anie.202200369.
[28] W.H. Zeng, L.Y. Wu, Y. Ishigaki, T. Harimoto, Y.X. Hu, Y.D. Sun, Y.Q. Wang, T. Suzuki, H.Y. Chen, D.J. Ye, An activatable afterglow/mri bimodal nanoprobe with fast response to hs for in *vivo* imaging of acute hepatitis, Angew. Chem. Int. Ed. 61 (2022) e202111759, https://doi.org/10.1002/anie.202111759.
[29] H. Bai, Y.Q. Wang, Y.X. Hu, D.J. Ye, A caspase-3-activatable bimodal probe for photoacoustic and magnetic resonance imaging of tumor apoptosis in *vivo*, Biosens. Bioelectron. 216 (2022) 114648, https://doi.org/10.1016/j.bios.2022.114648.
[30] H. Unterweger, C. Janko, M. Schwarz, L. Dézsi, R. Urbanics, J. Matuszak, E. Orfi, T. Fülöp, T. Bäuerle, J. Szebeni, C. Journé, A.R. Boccaccini, C. Alexiou, S. Lyer, I. Cicha, Non-immunogenic dextran-coated superparamagnetic iron oxide nanoparticles: a biocompatible, size-tunable contrast agent for magnetic resonance imaging, Int. J. Nanomed. 12 (2017) 5223–5238, https://doi.org/10.2147/Ijn.S138108.

[31] M. Wu, D. Zhang, Y.Y. Zeng, L.J. Wu, X.L. Liu, J.F. Liu, Nanocluster of superparamagnetic iron oxide nanoparticles coated with poly (dopamine) for magnetic field-targeting, highly sensitive MRI and photothermal cancer therapy, Nanotechnology 26 (2015) 115102, https://doi.org/10.1088/0957-4484/26/11/115102.
[32] Y.S. Liu, Y. Li, S. Koo, Y. Sun, Y.X. Liu, X. Liu, Y.N. Pan, Z.Y. Zhang, M.X. Du, S. Y. Lu, X. Qiao, J.F. Gao, X.B. Wang, Z.X. Deng, X.L. Meng, Y.L. Xiao, J.S. Kim, X. C. Hong, Versatile types of inorganic/organic nir-iia/iib fluorophores: from strategic design toward molecular imaging and theranostics, Chem. Rev. 122 (2022) 209–268, https://doi.org/10.1021/acs.chemrev.1c00553.
[33] L. Tu, C.L. Li, X.X. Xiong, J.H. Kim, Q. Li, L.C. Mei, J.R. Li, S. Liu, J.S. Kim, Y. Sun, Engineered metallacycle-based supramolecular photosensitizers for effective photodynamic therapy, Angew. Chem. Int. Ed. 62 (2023) e202301560, https://doi.org/10.1002/anie.202301560.
[34] Y. Qin, X.H. Chen, Y.X. Gui, H. Wang, B.Z. Tang, D. Wang, Self-assembled metallacage with second near-infrared aggregation-induced emission for enhanced multimodal theranostics, J. Am. Chem. Soc. 144 (2022) 12825–12833, https://doi.org/10.1021/jacs.2c03895.
[35] G.S. Hong, A.L. Antaris, H.J. Dai, Near-infrared fluorophores for biomedical imaging, Nat. Biomed. Eng. 1 (2017) 0010, https://doi.org/10.1038/s41551-016-0010.
[36] Y.T. Zhong, Z.R. Ma, F.F. Wang, X. Wang, Y.J. Yang, Y.L. Liu, X. Zhao, J.C. Li, H. T. Du, M.X. Zhang, Q.H. Cui, S.J. Zhu, Q.C. Sun, H. Wan, Y. Tian, Q. Liu, W. Z. Wang, K.C. Garcia, H.J. Dai, In vivo molecular imaging for immunotherapy using ultra-bright near-infrared-IIb rare-earth nanoparticles, Nat. Biotechnol. 37 (2019) 1322–1331, https://doi.org/10.1038/s41587-019-0262-4.
[37] J. Cui, F. Zhang, D.Y. Yan, T. Han, L. Wang, D. Wang, B.Z. Tang, "Trojan Horse" Phototheranostics: fine-engineering NIR-II AIEgen camouflaged by cancer cell membrane for homologous-targeting multimodal imaging-guided phototherapy, Adv. Mater. 35 (2023) 2302639, https://doi.org/10.1002/adma.202302639.
[38] D. Chen, J.L. Luo, C. Zhang, L.S. Tang, H. Deng, T.D. Chang, H.Q. Xu, M.B. He, D. L. Wan, F.Y. Zhang, M.F. Wu, M. Qian, W. Zhou, G. Yin, W.G. Wang, L.M. Dong, Z. H. Tang, Venous thrombus embolism in polytrauma: special attention to patients with traumatic brain injury, J. Clin. Med. 12 (2023) 1716, https://doi.org/10.3390/jcm12051716.
[39] Z.H. Lin, Y.Q. Lu, P. Artal, Z.K. Yang, W.Z. Lan, Two-dimensional peripheral refraction and image quality for four types of refractive surgeries, J. Refract. Surg. 39 (2023) 40–47, https://doi.org/10.3928/1081597x-20221115-01.
[40] T. Zhang, J. Zhang, F.-B. Wang, H. Cao, D. Zhu, X. Chen, C. Xu, X. Yang, W. Huang, Z. Wang, J. Wang, Z. He, Z. Zheng, J.W.Y. Lam, B.Z. Tang, Mitochondria-targeting phototheranostics by aggregation-induced nir-ii emission luminogens: modulating intramolecular motion by electron acceptor engineering for multi-modal synergistic therapy, Adv. Funct. Mater. 32 (2022) 2110526, https://doi.org/10.1002/adfm.202110526.
[41] Y.L. Xu, C.L. Li, X. Ma, W. Tuo, L. Tu, X.P. Li, Y. Sun, P.J. Stang, Y. Sun, Long wavelength-emissive Ru(II) metallacycle-based photosensitizer assisting in vivo bacterial diagnosis and antibacterial treatment, Proc. Natl. Acad. Sci. USA 119 (32) (2022) e2209904119, https://doi.org/10.1073/pnas.2209904119.
[42] D. Xu, J. Hao, H. Gao, Y. Wang, Y. Wang, X. Liu, A. Han, C. Zhang, Twisted donor–acceptor cruciform fluorophores exhibiting strong solid emission, efficient aggregation-induced emission and high contrast mechanofluorochromism, Dyes Pigments. 150 (2018) 293–300, https://doi.org/10.1016/j.dyepig.2017.12.031.
[43] J. Li, N. Niu, D. Wang, X. Liu, Y. Qin, L. Wang, B.Z. Tang, D. Wang, Acceptor-engineering tailored type-I photosensitizer with aggregation-induced NIR-II emission for cancer multimodal phototheranostics, Sci. China Chem. 67 (2024) 2647–2660, https://doi.org/10.1007/s11426-024-1980-x.
[44] J. Mei, N. Leung, R.T.K. Kwok, J.W.Y. Lam, B.Z. Tang, Aggregation-induced emission: together we shine, united we soar!, Chem. Rev. 115 (2015) 11718–11940, https://doi.org/10.1021/acs.chemrev.5b00263.
[45] T. Qiu, Y. Zhao, W.-S. Tang, H. Tan, H. Sun, Z. Kang, X. Zhao, Y. Li, Smart covalent organic framework with proton-initiated switchable photocatalytic aerobic oxidation, ACS Catal. 12 (2022) 12398–12408, https://doi.org/10.1021/acscatal.2c03796.
[46] W. Chen, Y. Zhang, H. Yi, F. Wang, X. Chu, J.-H. Jiang, Type I photosensitizer targeting g-quadruplex rna elicits augmented immunity for cancer ablation, Angew. Chem. Int. Ed. 62 (2023) e202300162, https://doi.org/10.1002/anie.202300162.
[47] Y.-Z. Peng, G.-C. Guo, S. Guo, L.-H. Kong, T.-B. Lu, Z.-M. Zhang, Charge transfer from donor to acceptor in conjugated microporous polymer for enhanced photosensitization, Angew. Chem. Int. Ed. 60 (2021) 22062–22069, https://doi.org/10.1002/anie.202109968.
[48] Y. Peng, W.X. Mei, K.D. Ma, C.C. Zeng, Circulating tumor dna and minimal residual disease (mrd) in solid tumors: current horizons and future perspectives, Front. Oncol. 11 (2021) 763790, https://doi.org/10.3389/fonc.2021.763790.